




Article

Gas Transport Arising from the Decomposition of Methane Hydrates in the Sediments of the Arctic Shelf to the Atmosphere: Numerical Modeling

Mariia Trimonova ^{*}, Nikolay Baryshnikov  and Sergey Turuntaev 

Sadovsky Institute of Geosphere Dynamics Russian Academy of Sciences, 119334 Moscow, Russia; baryshnikov.na@idg.ras.ru (N.B.); stur@idg.ras.ru (S.T.)

* Correspondence: trimonova.ma@gmail.com

Abstract: This study investigates the transport of methane released from gas hydrate decomposition through sedimentary layers to quantify its flux into the atmosphere, a critical process given methane's role as a major greenhouse gas. A novel methodology was developed to model two-phase, unsteady gas flow in regions of hydrate decomposition, incorporating key factors such as relative permeability curves, capillary pressure, hydrostatics, and gas diffusion. Numerical simulations revealed that to achieve a gas front rise rate of 7 m/year, the gas accumulation rate must not exceed 10^{-8} kg/m³·s. At higher accumulation rates (10^{-6} kg/m³·s), gas diffusion has minimal impact on the saturation front movement, whereas at lower rates (10^{-8} kg/m³·s), diffusion significantly affects the front's behavior. The study also established that the critical gas accumulation rate required to trigger sediment blowout in the hydrate decomposition zone is approximately 10^{-6} kg/m³·s, several orders of magnitude greater than typical bubble gas fluxes observed at the ocean surface. The proposed model improves the ability to predict the contribution of Arctic shelf methane hydrate decomposition to atmospheric methane concentrations.

Keywords: numerical simulation; methane hydrate; sediment blowouts; two-phase flow; gas accumulation rate; relative permeability; capillary pressure; gas diffusion



Academic Editor: Yoshizumi Kajii

Received: 2 December 2024

Revised: 20 December 2024

Accepted: 23 December 2024

Published: 26 December 2024

Citation: Trimonova, M.; Baryshnikov, N.; Turuntaev, S. Gas Transport Arising from the Decomposition of Methane Hydrates in the Sediments of the Arctic Shelf to the Atmosphere: Numerical Modeling. *Atmosphere* **2025**, *16*, 9. <https://doi.org/10.3390/atmos16010009>

Copyright: © 2024 by the authors. Licensee MDPI, Basel, Switzerland. This article is an open access article distributed under the terms and conditions of the Creative Commons Attribution (CC BY) license (<https://creativecommons.org/licenses/by/4.0/>).

1. Introduction

The science of gas hydrates has existed for the last two centuries. By the end of the last century, its main applied tasks included the prevention and elimination of gas hydrate blockages in pipelines, as well as the exploration of gas hydrates as an unconventional source of hydrocarbon raw materials [1–3]. Over the past thirty years, particular attention has been paid to studying factors influencing global climate change. One “underappreciated” factor that may contribute to this is the presence of methane hydrate deposits, which, when decomposed, release methane into the atmosphere. Recent studies show that, on the one hand, global warming has a much stronger effect on increasing methane emissions into the atmosphere than previously thought [4,5]. On the other hand, the impact of increasing methane concentration in the atmosphere on global warming has also been underestimated [6]. The observed rate of warming exceeds the predictions of climate models, likely due to numerous feedback loops not included in the calculations. Additionally, the isotopic composition of atmospheric methane indicates that methane emissions from the use of natural gas have not been the dominant factor behind the increase in methane concentrations in the 21st century [7,8]. At the same time, global greenhouse gas emissions from natural sources remain poorly studied and inadequately reflected in

most modern climate models [9,10]. For example, current methane emission estimates do not account for the gas released into the atmosphere from permafrost thawing in the Arctic, despite the fact that it is known the potential for methane emissions from deep cryosphere sources is significant [11]. Therefore, to accurately assess the causal relationships behind global warming and quantitatively evaluate non-anthropogenic greenhouse gas emissions, a more detailed understanding of the physical processes occurring in the upper layers of sedimentary rocks in the Earth's crust, particularly in the cryolithozone, is necessary.

The object of this study is the gas transport process resulting from the decomposition of gas hydrates in the seabed deposits of the East Siberian Arctic Shelf, from the point of their formation to the seafloor surface. According to estimates [12], up to 57% of the seabed deposits of the East Siberian Arctic Shelf may contain methane gas hydrates, which exist within the so-called stability zone [13,14]. The boundaries of this zone are determined by the thermobaric conditions necessary for hydrate stability. For instance, at temperatures around 0 °C, gas hydrates are stable at pressures above 2.5 MPa. In the seabed deposits of the continental shelf, this pressure is provided by the total hydrostatic and lithostatic pressure of the overlying sedimentary rock layers and water. The depth at which hydrates are found relative to the seafloor can range from 0 to approximately 100 m or more, depending on local thermobaric conditions. With changes in temperature regimes, gas hydrates may lose their stability, partially transitioning into free gas, which is then transported to the surface. The mechanism of gas transport within sedimentary rocks is still poorly understood. Depending on pressure and temperature conditions, the gas released during the decomposition of hydrates may exist in both free and dissolved forms. Gas bubbles rising from the seafloor suggest that there is an area of gas release and accumulation in free form beneath the surface, from which the gas is further transported to the water column above the seafloor [15,16]. The mechanism of this transport remains insufficiently explored in the literature [17]. Typically, diffusion and advective mechanisms [18–22], free gas flux due to excess pressure [22], or the movement of gas in the form of separate microbubbles [5,23] are discussed. This problem has several distinctive features compared to traditional studies of multiphase flows that arise during oil and gas production. First and foremost, these include the extremely low characteristic hydrodynamic pressure gradients. Under such conditions, the flow velocity and phase distribution in the pore space are determined not only by resistance from the sedimentary rock matrix but also by interactions between the phases. Gas penetrates through the water-saturated medium, which is in hydrostatic equilibrium, with capillary forces playing a key role. The resistance to gas flow caused by capillary forces may lead to the accumulation of excess pressure beneath the seafloor surface. Since seabed sediments are usually unconsolidated (e.g., clayey sands) and are located at shallow depths, localized seabed uplift (so-called “pingo” formations) [24,25] or even ejections of sediment with crater formation [15,26] may occur.

In this study, we examine the problem of unstable two-phase gas flow from the site of its formation to the seafloor surface under field conditions [27]. We consider the consequences of a gas hydrate moving out of its stability zone due to changes in external conditions, such as an increase in temperature or a decrease in ocean level, which leads to a reduction in pore pressure at the location of the gas hydrate (Figure 1).

The modeling was conducted with consideration of the effects of capillary pressure, hydrostatic pressure gradients in both gas and liquid phases, specific forms of relative permeability curves, and the influence of gas diffusion. The study aimed to determine how the properties of the medium and fluids, as well as the rate of gas release at the source, affect the rate of the gas front's advancement toward the seafloor surface. Additionally, we investigated the potential for sediment blowouts caused by the accumulation of excess gas pressure at certain depths.

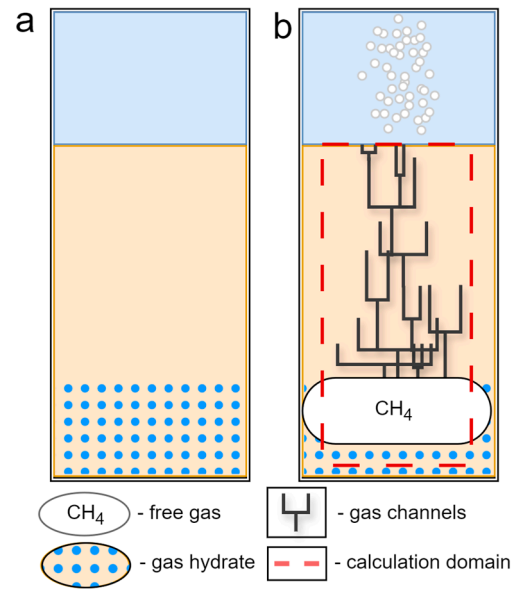


Figure 1. Schematic representation of the investigated process: (a)—hydrate in the seabed; (b)—after the loss of stability (white particles—gas bubbles, blue area—sea water).

2. Problem Statement

2.1. Mathematical Model

In works [28,29], the authors analyzed a single-phase gas flow model in a rock, both in one-dimensional and two-dimensional setups. The present study builds on these works by extending the analysis to two-phase gas flow in a water layer within a three-dimensional framework. Unlike the studies in [28,29], where the Leibenson equation was solved numerically, this work develops a comprehensive approach to solving a system of fundamental equations, including the continuity equation, the momentum equation, and the corresponding closure relations. The study focuses on the combined isothermal flow of two phases in a homogeneous, incompressible porous medium, excluding phase transitions and chemical reactions.

The mass conservation laws for the gas and the liquid phases are expressed as follows:

$$m \frac{\partial(\rho_1 s)}{\partial t} + \text{div}(\rho_1 \vec{v}_1) = q \tag{1}$$

$$m \frac{\partial(\rho_2(1-s))}{\partial t} + \text{div}(\rho_2 \vec{v}_2) = 0 \tag{2}$$

The equations of motion for both phases are formulated using Darcy’s law are the following:

$$\vec{v}_1 = -\frac{k}{\mu_1} k_1(s) (\nabla P_1 - \rho_1 \vec{g}) \tag{3}$$

$$\vec{v}_2 = -\frac{k}{\mu_2} k_2(s) (\nabla P_2 - \rho_2 \vec{g}) \tag{4}$$

The equations of state define the relationship between the phase densities and the pressure. In this model, the liquid is considered incompressible, and its density is independent of pressure, i.e.:

$$\rho_2 = \text{const} \tag{5}$$

At the same time, it is assumed that the gas density varies linearly with pressure, as follows:

$$\rho_1 = P_1 \frac{\rho_{10}}{P_{10}} \tag{6}$$

The model incorporates capillary forces acting between the fluid and gas phases. As a result, the pressures of the two phases are related by the following:

$$P_2 - P_1 = P_c = const \tag{7}$$

here m —matrix porosity, ρ_1 —gas density, ρ_2 —liquid density, \vec{v}_1 —gas flow rate, \vec{v}_2 —liquid flow rate, s —gas saturation, $(1 - s)$ —liquid saturation, k —absolute matrix permeability, $k_i(s)$ —relative permeabilities of the gas ($i = 1$) and liquid ($i = 2$) phases, μ_i —dynamic viscosities of the gas and liquid phases, P_i —pressures of the gas ($i = 1$) and liquid ($i = 2$), \vec{g} —gravitational acceleration vector, ρ_{10} —initial gas density, P_{10} —initial gas pressure, P_c —capillary pressure, q —gas accumulation rate.

The relative phase permeabilities are functions of saturation, expressed as follows: $k_1(s) = \frac{s-s^*}{1-s^*}$, $k_2(s) = 1 - s$. For the gas phase, there exists a minimum movable saturation, denoted as s^* . Below this value, the relative phase permeability for the gas is zero, and for higher values, it increases linearly with the gas saturation s .

Expanding the derivative of the product in the continuity equation for the gas (1) and factoring out the liquid density in Equation (2), we obtain:

$$s \frac{\partial \rho_1}{\partial t} + \rho_1 \frac{\partial s}{\partial t} = -\frac{1}{m} \operatorname{div}(\rho_1 \vec{v}_1) \tag{8}$$

$$\frac{\partial s}{\partial t} = \frac{1}{m} \operatorname{div}(\vec{v}_2) \tag{9}$$

By substituting Equation (8) into Equation (7) and considering the dependence of the flow rates of the liquid and gas on pressure (as given by Equations (3) and (4)), we obtain a system of equations that describes the state of the medium, including the variation in the distribution of gas and liquid densities/pressures and the saturation profile:

$$\begin{cases} \frac{\partial s}{\partial t} = \frac{1}{m} \operatorname{div}(\vec{v}_2) \\ \frac{\partial \rho_1}{\partial t} = -\frac{1}{sm} \left(\vec{v}_1 * \operatorname{div}(\rho_1) + \rho_1 \left(\operatorname{div}(\vec{v}_1) + \operatorname{div}(\vec{v}_2) \right) \right) \\ \vec{v}_1 = -\frac{k}{\mu_1} k_1(s) \left(\nabla P_1 - \rho_1 \vec{g} \right) \\ \vec{v}_2 = -\frac{k}{\mu_2} k_2(s) \left(\nabla P_2 - \rho_2 \vec{g} \right) \end{cases} \tag{10}$$

In determining the divergence of the flow rates, the dependence of the relative phase permeability on saturation is incorporated. For each phase this relationship is given by:

$$\operatorname{div}(\vec{v}_i) = -k \frac{k_i(s)}{\eta_i} \Delta P_i - \frac{k}{\mu_i} \left(\nabla P_i - \rho_i \vec{g} \right) \cdot \nabla k_i(s), i = 1, 2 \tag{11}$$

To solve the system of differential equations, it is necessary to define initial and boundary conditions, which are typically expressed as follows:

$$\begin{cases} s(t = 0) = s_0 \\ P(t = 0) = P_0 \\ s(x, y, z - bound) = s_{bound} \\ P(x, y, z - bound) = P_{bound} \end{cases} \tag{12}$$

The specific form of the initial and boundary conditions depends on the problem formulation.

2.2. Input Data

This study establishes the conditions based on field research [27]: geometry of the computational domain, boundary and initial conditions, and medium properties. During expeditions aimed at studying the potential methane release zone in the Laptev Strait, high-precision seismic surveys of the seabed were conducted, accompanied by selective drilling in areas with high concentrations of dissolved methane in seawater. The results revealed cross-sections with low-amplitude anomalies, typical for sedimentary rocks containing significant amounts of free gas in their pores. Over the course of the year between observations, the upper boundary of some areas moved upward at a rate of 7 m/year, while other areas remained stationary. Drilling results indicated that methane concentrations in the anomalous zones were approximately $4 \times 10^3 \mu\text{M/L}$, two orders of magnitude higher than typical values. The original study concluded that these zones represent a “front” of gas rising from the sediment layers. It is assumed that the mobile zones with free gas are likely forming gas channels, while the stationary areas are “impermeable” under hydrostatic gradients. The gas concentration in the sedimentary rock samples was approximately 1.6 times higher than the maximum concentration of dissolved methane under the given thermobaric conditions ($2.48 \times 10^3 \mu\text{M/L}$).

To model these field conditions, the computational domain is represented as a rectangle:

This is the subsurface area filled with liquid (water) and gas (CH_4). The y-axis represents depth, with the seabed considered to be at the top.

2.3. Initial Conditions

Figure 2 shows the distribution of gas saturation in the sediments at the initial state. According to data from the expedition, there is an area within the sedimentary rock where gas has accumulated. This means the gas saturation in this area is higher than in the rest of the domain. This area is highlighted in yellow in Figure 2. The initial gas saturation in the gas accumulation area, along with the absolute and relative permeability and porosity of the matrix, were taken from the papers by Chuvilin [30,31], which separately investigated sedimentary rock samples taken from the wells. The initial gas saturation in the remaining part of the computational domain was set to a relatively small value (0.05). The initial gas density is set to the density of CH_4 at the initial pressure conditions. The initial pressure distribution accounted for the gravitational force acting within the water and gas column in the computational domain, as well as the weight of the water column acting from above on the seabed. The Table 1 below lists the input and initial parameters for the problem under consideration.

Table 1. Input and initial parameters.

Title	Values
The domain size along the X-axis, m	4
The domain size along the Y-axis, m	16
The domain size along the Z-axis, m	1
Gas density, kg/m^3	1.28
Fluid density, kg/m^3	1000
Gas viscosity, cP	0.01
Fluid viscosity, cP	1
Rock permeability, D	0.1
Porosity	0.5
Initial gas saturation	0.05
Minimum movable saturation	0.2
Capillary pressure, MPa	0.001
Sea depth, m	3

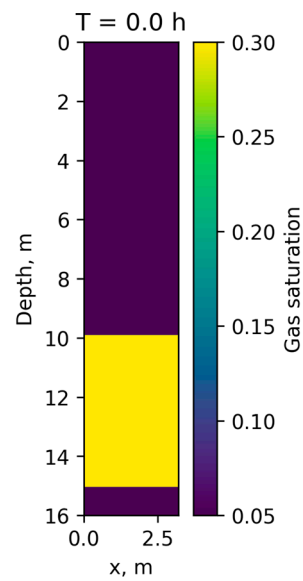


Figure 2. Computational domain with initial gas saturation distribution.

It is important to note that, in reality, permeability is unlikely to be strictly uniform across the entire domain. Therefore, in our model, a random distribution centered around a value of 0.1 D was applied, accounting for the layered structure of the medium. The permeability distribution used in the calculations is presented in Figure 3.

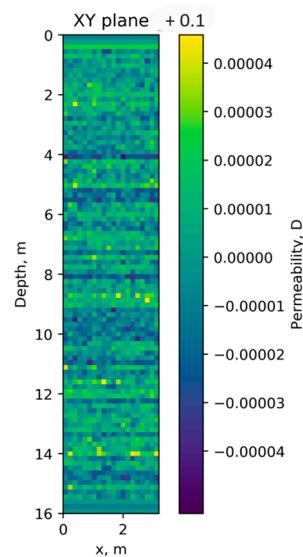


Figure 3. The permeability distribution used in the calculations.

The capillary pressure P_c , presented in Table 1, was determined using the formula: $P_c = 2 * \alpha / r$ where α is the surface tension coefficient between gas and water, and r is the pore size defined in Chuvilin's work [30,31]. It was assumed that $\alpha = 0.04$ and $r = 0.08$ mm, which resulted in a capillary pressure of approximately 1000 Pa.

In addition to the input parameters, the study assumed that at the initial time, gas begins to penetrate the medium from the yellow zone (Figure 2) with an increased gas content, at a constant accumulation rate q , which is included in the system of Equation (10) and physically represents the mass of gas entering a unit volume per unit of time. To convert the volumetric gas accumulation rate to the areal rate, the value ($\text{kg}/\text{m}^3/\text{s}$) should be multiplied by the height of the region with increased gas saturation.

2.4. Boundary Conditions

Neumann boundary conditions were applied to the left and right boundaries for pressure: the flow rate (according to Darcy's law) was set to zero. A Dirichlet boundary condition was applied to the upper boundary, where the pressure was kept constant and equal to the weight of the water column. A Neumann boundary condition was also applied to the lower boundary, where the pressure derivative was set to $\rho_2 \vec{g}$.

The computational domain was three-dimensional. However, for this study, a small thickness of two grid cells was assigned along the Z-axis. Zero flow rate boundary conditions were applied at the boundaries along the X-axis as well.

To solve the system of Equation (10), the Py-pde library [32] was used.

2.5. Objective of the Study in Detail

The objective of this work was to investigate the real conditions of gas flux, determine the possible conditions for the formation of gas blowouts within the sedimentary rock, evaluate the impact of capillary forces P_c and minimum movable saturation s^* on the gas flux process, as well as examine the potential influence of gas diffusion into the sedimentary rock.

Real conditions refer to the conditions found by the authors in works [27,30,31] and presented in Table 1. A gas blowout is defined as the failure of rock due to liquid pressure exceeding the weight of the overlying rock. To model this, the change in the distribution of gas pressure over time within the computational domain was determined by solving the system of Equation (10). At each time step, the pressure at every point within the domain was compared to the weight of the overlying rock acting on it. If the pressure exceeded the rock's weight, it was concluded that the rock would fail at that point. The authors have previously investigated this process in simpler versions of the mathematical model (one-dimensional, two-dimensional, single-phase) [28,29].

Gas diffusion is understood as the process of gas movement not only vertically due to the buoyant force but also in all directions due to the mixing of the gas [18]. To study the influence of diffusion, terms accounting for gas diffusion were added to the mass conservation Equations (1) and (2):

$$m \frac{\partial(\rho_1 s)}{\partial t} + \text{div}(\rho_1 \vec{v}_1) = q + \rho_1 m D \Delta s \quad (13)$$

$$m \frac{\partial(\rho_2(1-s))}{\partial t} + \text{div}(\rho_2 \vec{v}_2) = \rho_2 m D \Delta(1-s) \quad (14)$$

where D is the diffusion coefficient, the value of which ($5 \times 10^{-10} \text{ m}^2/\text{s}$) was determined in [18]. By following the same procedure with the mass conservation and motion equations as in the derivation of the system of Equation (10), it was found that the term corresponding to diffusion appears in the final form of the equation for the change in saturation:

$$\frac{\partial s}{\partial t} = \frac{1}{m} \text{div}(\vec{v}_2) + D \Delta s \quad (15)$$

2.6. Convergence Study

Before performing the calculations, it was necessary to select the optimal time step and grid resolution. While the time step in the used library is automatically determined and the calculation duration does not depend on the number of time steps for a given total time, the grid resolution affects both the calculation time and the quality of the results. Therefore, for the input parameters from Table 1 and a gas accumulation rate q of $10^{-6} \text{ kg/m}^3/\text{s}$ the grid was refined, and the results were compared. Additionally, the permeability for the

grid with a step size of 16 cm along the X and Y axes, shown in Figure 3, was interpolated onto a finer grid with a step size of 8 cm along the same axes.

The change in saturation over time for the two grids is shown in Figure 4.

Some difference can be observed, but the evolution of the depth of the front of average gas saturation over time for the two grids shows similar patterns (Figure 5). The average saturation was determined by averaging the saturation along the X and Z axes.

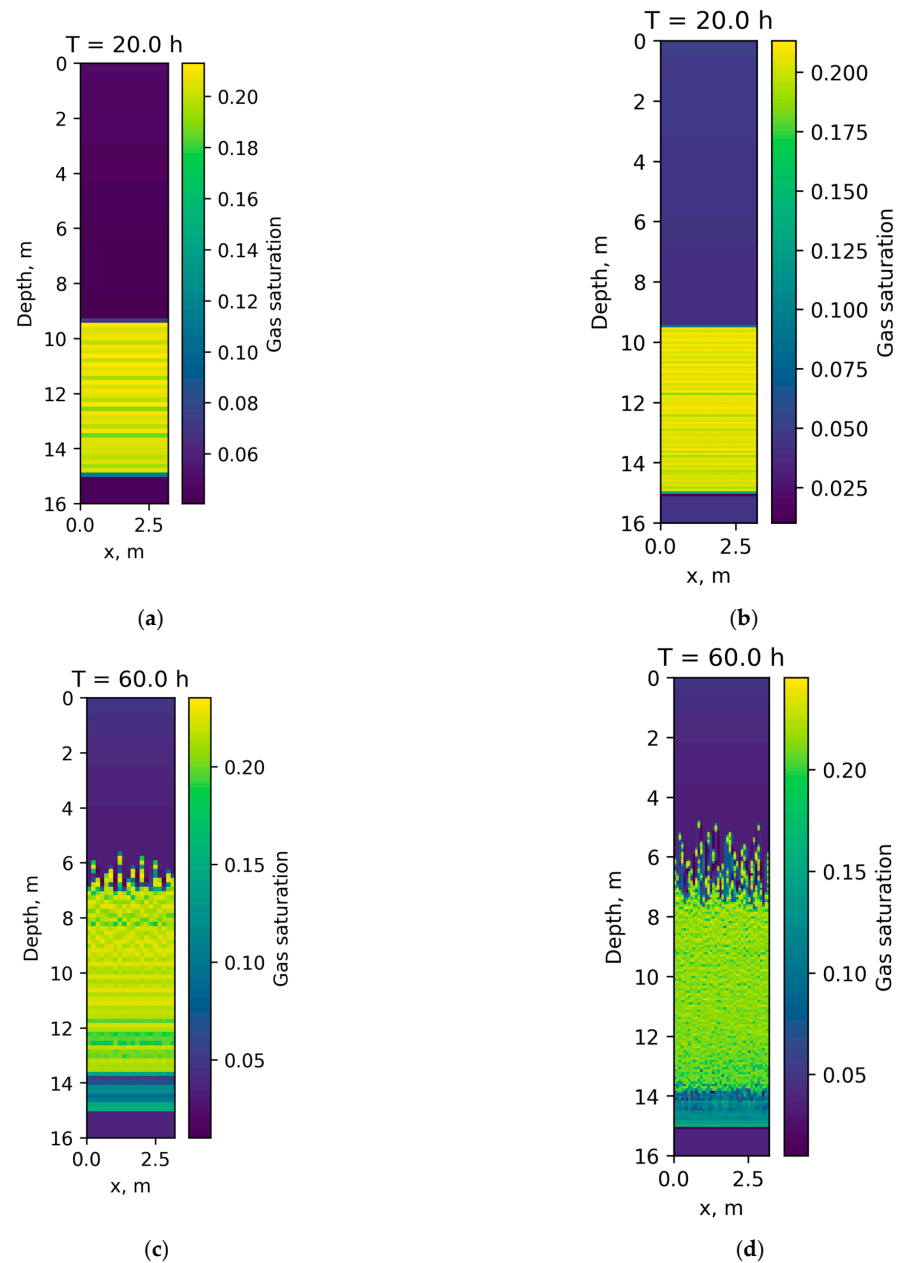


Figure 4. Cont.

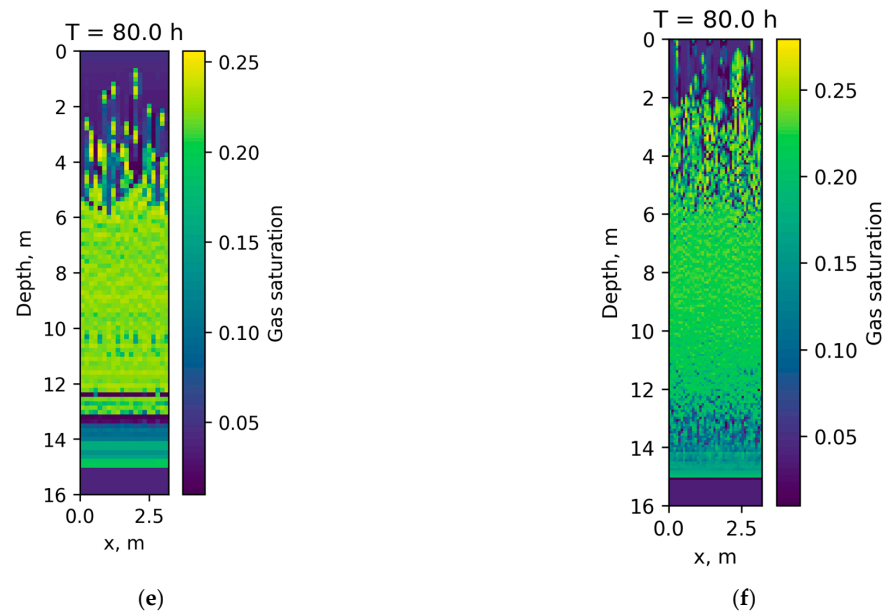


Figure 4. The change in saturation over time for the two grids: (a,c,e)—for big grid; (b,d,f)—for tiny grid ((a,b)—after 20 h; (c,d)—after 60 h; (e,f)—after 80 h).

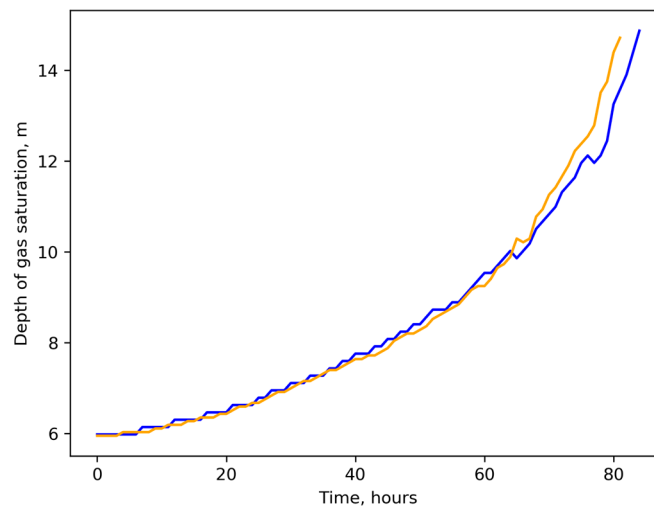


Figure 5. Evolution of the depth of the front of average gas saturation over time (blue—big grid, orange—small grid).

Therefore, to increase the calculation speed, it was decided to perform all calculations on a grid with a step size of 16 cm along both the X and Y axes.

3. Results

The calculations were carried out for three different gas accumulation rates: $q = 10^{-6}$, 10^{-7} , 10^{-8} kg/m³ /s. For each of these accumulation rates, two values of the gas diffusion coefficient were used: $D = 5 \times 10^{-10}$ and 5×10^{-9} m²/s. Additionally, the capillary pressure P_c and the minimum mobile saturation s^* were varied.

3.1. Influence of Input Parameters on the Gas Front Velocity

Almost all calculations were performed for a capillary pressure of 0.001 MPa. To study the influence of capillary pressure, calculations were also carried out for values of 0.18 MPa and 0.05 MPa. The capillary pressure was estimated based on the relationship between the pore radius and the matrix permeability and porosity, given by the equation: $r \simeq \sqrt{k/m}$. Because we are more often aware of the matrix permeability rather than the pore size. For

a permeability of 0.1 D and porosity of 0.5, the capillary pressure (was calculated to be 0.18 MPa).

Similarly, all calculations were carried out with $s^* = 0.2$, and to examine its effect, calculations were also made for $s^* = 0.3$. Other calculation parameters were taken from Table 1.

An example of the saturation distribution in the computational domain for different parameters is provided below. We attempted to place the figures of the results with one differing parameter in adjacent cells for easier comparison.

Figure 6a,b show the difference in saturation movement depending on the gas accumulation rates (10^{-6} , 10^{-7} kg/m³/s) after 80 h from the start. Figure 6a–c,f illustrate the effect of the diffusion coefficient on the change in saturation in the medium at different accumulation rates. It is evident that at a significantly higher accumulation rate (10^{-6} kg/m³/s), the influence of the diffusion coefficient is much smaller compared to a lower rate of 10^{-8} kg/m³/s. Figure 6b,e demonstrate the impact of varying capillary pressures. Higher capillary pressure results in a slowdown of the saturation front movement.

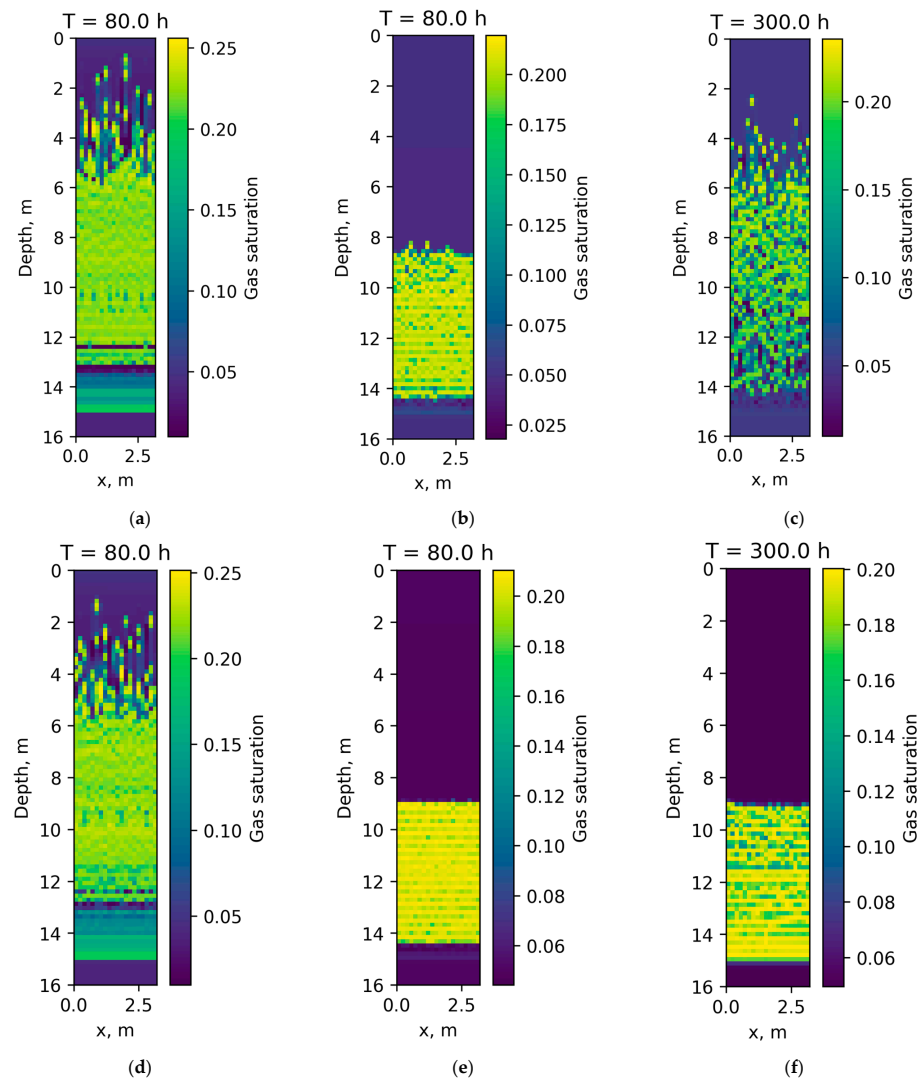


Figure 6. Saturation distribution in the computational domain for different parameters: (a) $D = 5 \times 10^{-10}$ m²/s, $P_c = 0.001$ MPa, $q = 10^{-6}$ kg/m³/s, $s^* = 0.2$; (b) $D = 5 \times 10^{-10}$ m²/s, $P_c = 0.001$ MPa, $q = 10^{-7}$ kg/m³/s, $s^* = 0.2$; (c) $D = 5 \times 10^{-10}$ m²/s, $P_c = 0.001$ MPa, $q = 10^{-6}$ kg/m³/s, $s^* = 0.2$; (d) $D = 5 \times 10^{-9}$ m²/s, $P_c = 0.001$ MPa, $q = 10^{-6}$ kg/m³/s, $s^* = 0.2$; (e) $D = 5 \times 10^{-10}$ m²/s, $P_c = 0.18$ MPa, $q = 10^{-7}$ kg/m³/s, $s^* = 0.2$; (f) $D = 5 \times 10^{-9}$ m²/s, $P_c = 0.001$ MPa, $q = 10^{-8}$ kg/m³/s, $s^* = 0.2$.

To make a more detailed comparison of all calculations not only at a specific moment in time but also over the entire duration of the calculations, a dependency of the depth of average saturation over time was constructed (Figure 7).

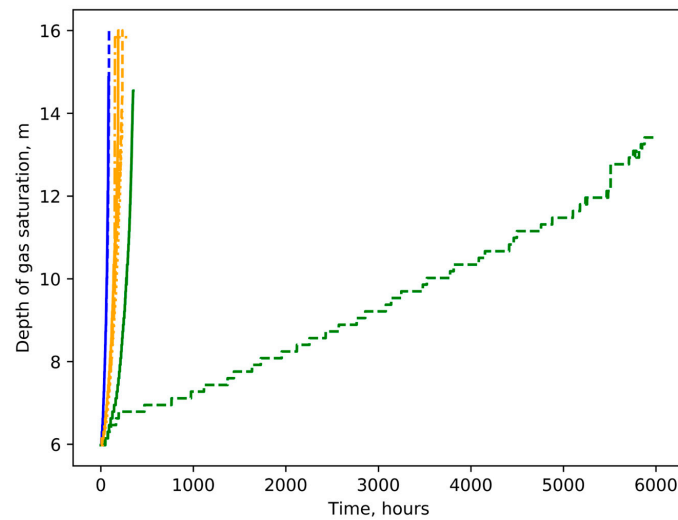


Figure 7. Dependency of the depth of average saturation over time: (blue)— $D = 5 \times 10^{-10} \text{ m}^2/\text{s}$, $P = 0.001 \text{ MPa}$, $q = 1 \times 10^{-6} \text{ kg/m}^3/\text{s}$; (orange)— $D = 5 \times 10^{-10} \text{ m}^2/\text{s}$, $P = 0.001 \text{ MPa}$, $q = 1 \times 10^{-7} \text{ kg/m}^3/\text{s}$; (green)— $D = 5 \times 10^{-10} \text{ m}^2/\text{s}$, $P = 0.001 \text{ MPa}$, $q = 1 \times 10^{-8} \text{ kg/m}^3/\text{s}$; (blue dashed)— $D = 5 \times 10^{-9} \text{ m}^2/\text{s}$, $P = 0.001 \text{ MPa}$, $q = 1 \times 10^{-6} \text{ kg/m}^3/\text{s}$; (orange dashed)— $D = 5 \times 10^{-9} \text{ m}^2/\text{s}$, $P = 0.001 \text{ MPa}$, $q = 1 \times 10^{-7} \text{ kg/m}^3/\text{s}$; (green dashed)— $D = 5 \times 10^{-9} \text{ m}^2/\text{s}$, $P = 0.001 \text{ MPa}$, $q = 1 \times 10^{-8} \text{ kg/m}^3/\text{s}$; (orange dotted)— $D = 5 \times 10^{-10} \text{ m}^2/\text{s}$, $P = 0.18 \text{ MPa}$, $q = 1 \times 10^{-7} \text{ kg/m}^3/\text{s}$; (orange dashed-dotted)— $D = 5 \times 10^{-10} \text{ m}^2/\text{s}$, $P = 0.001 \text{ MPa}$, $q = 1 \times 10^{-7} \text{ kg/m}^3/\text{s}$, $s^* = 0.3$.

Zooming the graph (Figure 8):

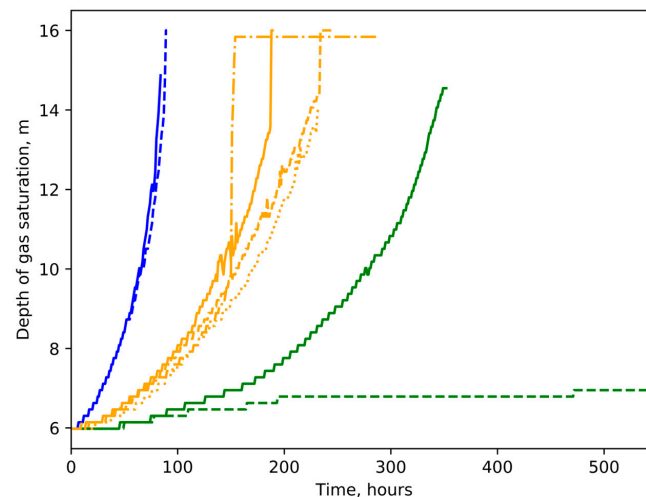


Figure 8. Dependency of the depth of average saturation over time: zooming Figure 7: (blue)— $D = 5 \times 10^{-10} \text{ m}^2/\text{s}$, $P = 0.001 \text{ MPa}$, $q = 1 \times 10^{-6} \text{ kg/m}^3/\text{s}$; (orange)— $D = 5 \times 10^{-10} \text{ m}^2/\text{s}$, $P = 0.001 \text{ MPa}$, $q = 1 \times 10^{-7} \text{ kg/m}^3/\text{s}$; (green)— $D = 5 \times 10^{-10} \text{ m}^2/\text{s}$, $P = 0.001 \text{ MPa}$, $q = 1 \times 10^{-8} \text{ kg/m}^3/\text{s}$; (blue dashed)— $D = 5 \times 10^{-9} \text{ m}^2/\text{s}$, $P = 0.001 \text{ MPa}$, $q = 1 \times 10^{-6} \text{ kg/m}^3/\text{s}$; (orange dashed)— $D = 5 \times 10^{-9} \text{ m}^2/\text{s}$, $P = 0.001 \text{ MPa}$, $q = 1 \times 10^{-7} \text{ kg/m}^3/\text{s}$; (green dashed)— $D = 5 \times 10^{-9} \text{ m}^2/\text{s}$, $P = 0.001 \text{ MPa}$, $q = 1 \times 10^{-8} \text{ kg/m}^3/\text{s}$; (orange dotted)— $D = 5 \times 10^{-10} \text{ m}^2/\text{s}$, $P = 0.18 \text{ MPa}$, $q = 1 \times 10^{-7} \text{ kg/m}^3/\text{s}$; (orange dashed-dotted)— $D = 5 \times 10^{-10} \text{ m}^2/\text{s}$, $P = 0.001 \text{ MPa}$, $q = 1 \times 10^{-7} \text{ kg/m}^3/\text{s}$, $s^* = 0.3$.

To avoid cluttering the figure, calculations are shown for $s^* = 0.2$ and $P_c = 0.001$ MPa, while for $s^* = 0.3$ and $P_c = 0.18$ MPa, only one calculation is included. The lines in the figure that have the same color represent the same flow rates.

The average velocity of the gas saturation front can be defined as the time it takes for the front to reach the top of the domain. The relationship between this velocity and the gas accumulation rate from the area with increased gas concentration (the yellow area in Figure 2) for all calculations is presented in Figure 9.

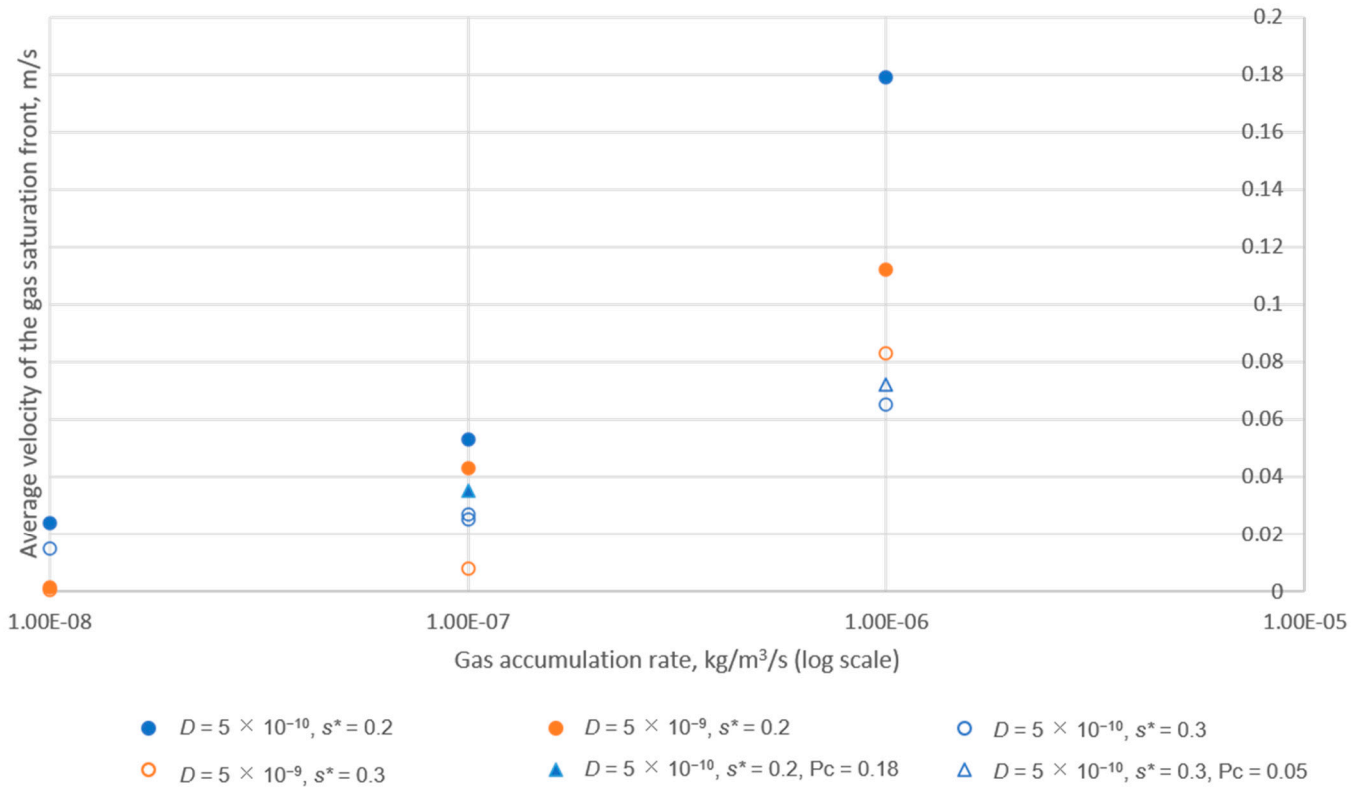


Figure 9. Dependency of the average velocity of the gas saturation front on the gas accumulation rate.

As a result, it was found that the saturation front velocity, equal to one presented in the article [27] (7 m per year) corresponds to a gas accumulation rate q of 10^{-8} kg/m³/s and is achieved with a diffusion coefficient D of 5×10^{-9} m²/s. For other parameter values, the velocity of the gas saturation front movement is significantly higher.

3.2. The Study of Potential Blowout Formation

It was found that under the given conditions (Table 1), blowouts occur only at gas accumulation rates of 10^{-6} kg/m³/s and 10^{-7} kg/m³/s. For the 10^{-8} kg/m³/s accumulation rate, variations in other parameters such as the diffusion coefficient and capillary pressure did not affect the formation of blowouts. However, at the accumulation rate of 10^{-7} kg/m³/s, the diffusion coefficient did have an impact: with a lower diffusion coefficient, blowouts occurred earlier. Meanwhile, variations in capillary pressure did not lead to differences in blowout formation, similar to the case with the 10^{-6} kg/m³/s accumulation rate.

Figure 10a,b,e,f,i,j show the initial moment of blowouts formation and gas saturation at that moment, while Figure 10c,d,g,h,k,l illustrate how the pressure profile and saturation profile in the computational domain change over time. However, it is important to note that after the initiation of blowouts, for the accumulation rate q of 10^{-6} kg/m³/s, calculating pressure and saturation is not correct, because in the areas where blowouts occur, the

permeability and density of the sedimentary rock change drastically. This process has not yet been accounted for in our model and is part of our future plans.

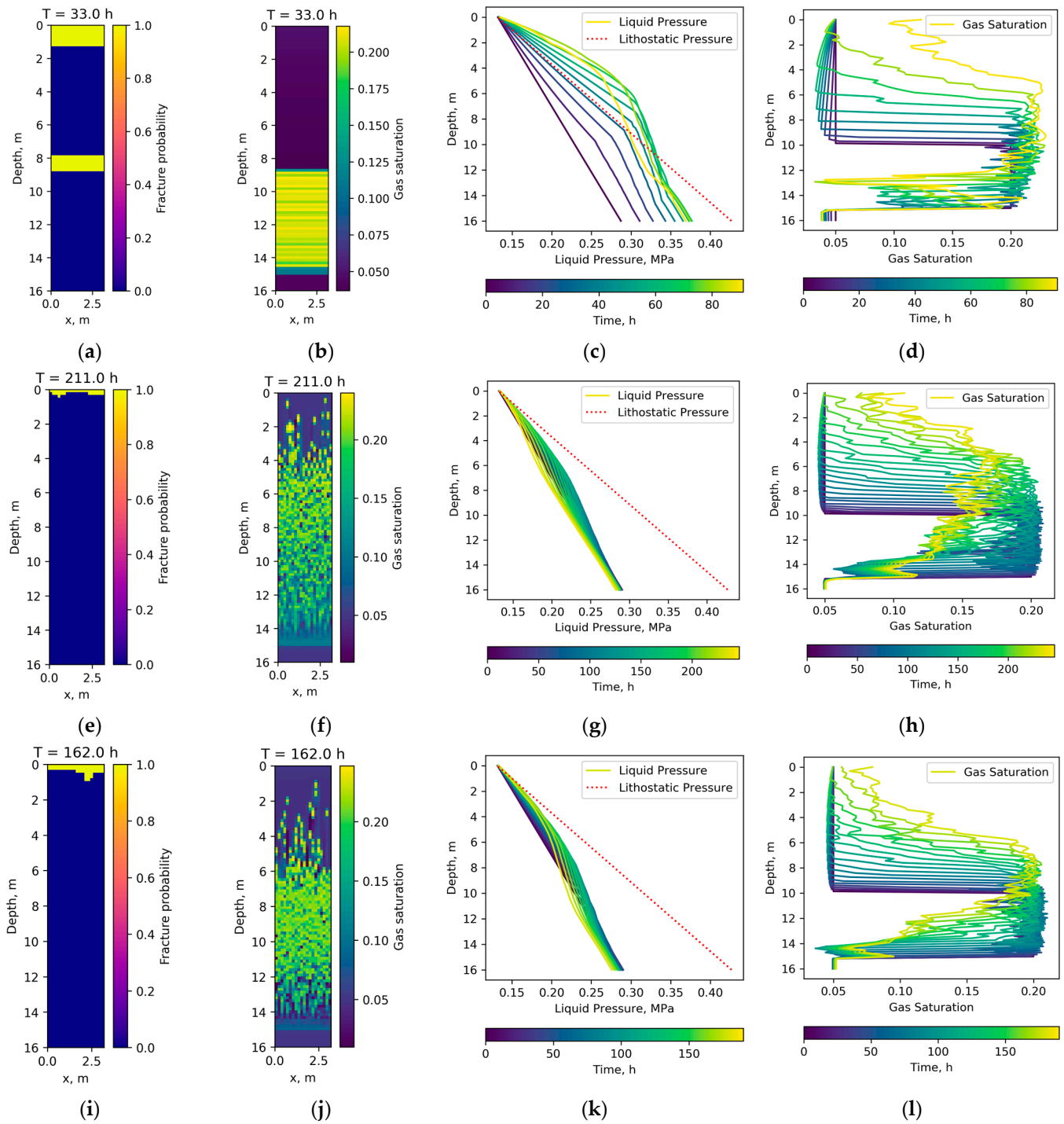


Figure 10. (a–d)— $D = 5 \times 10^{-9} \text{ m}^2/\text{s}$, $P_c = 0.001 \text{ MPa}$, $q = 10^{-6} \text{ kg}/\text{m}^3/\text{s}$, $s^* = 0.2$; (e–h)— $D = 5 \times 10^{-9} \text{ m}^2/\text{s}$, $P_c = 0.001 \text{ MPa}$, $q = 10^{-7} \text{ kg}/\text{m}^3/\text{s}$, $s^* = 0.2$; (i–l)— $D = 5 \times 10^{-10} \text{ m}^2/\text{s}$, $P_c = 0.001 \text{ MPa}$, $q = 10^{-7} \text{ kg}/\text{m}^3/\text{s}$, $s^* = 0.2$; (a,e,i)—blowout initiation moments for different parameters at different time steps; (b,f,j)—corresponding gas saturation; (c,g,k)—the change in pressure over time compared to the lithostatic pressure in the computational domain; (d,h,l)—the change in gas saturation over time in the computational domain.

4. Conclusions

In the work, a three-dimensional model of two-phase flow (gas + liquid) in rock from a gas accumulation zone is developed. By incorporating spatially variable permeability, the authors were able to simulate a realistic representation of two-phase gas flow in the sediments, specifically capturing the formation of gas “fingers”. During the simulation, parameters such as gas accumulation rates, diffusion coefficients, capillary pressures, and minimum movable saturations were varied. The following results were obtained from the simulation:

- (1) The parameters of the medium were identified under which the field conditions, obtained during expeditions [27], were recreated. It was found that to achieve a gas front rise rate of 7 m/year, the gas accumulation rate should be set to 10^{-8} kg/m³/s, and the diffusion coefficient to 5×10^{-9} m²/s.
- (2) The effect of the gas diffusion process on the gas front rise rate was determined. It was shown that at higher gas accumulation rates (10^{-6} kg/m³/s), diffusion has little impact on the saturation front movement, whereas at lower rates (10^{-8} kg/m³/s), it significantly affects the front movement.
- (3) It was found that increases in both capillary pressure and minimum movable saturation leads to a slowdown of the saturation front.
- (4) It was established that gas accumulation rates of 10^{-6} kg/m³/s and 10^{-7} kg/m³/s may lead to the formation of blowouts. It should be noted that these values are just several orders of magnitude higher than the average emission determined at the ocean surface.
- (5) A model was created that provides prediction of the contribution of methane hydrate decomposition to atmospheric emissions.

Author Contributions: Conceptualization, S.T.; methodology, S.T. and N.B.; software, N.B.; validation, M.T. and N.B.; formal analysis, N.B. and M.T.; investigation, M.T. and N.B.; resources, N.B. and M.T.; data curation, M.T. and N.B.; writing—original draft preparation, M.T.; writing—review and editing, N.B.; visualization, M.T. and N.B.; supervision, N.B. and S.T. All authors have read and agreed to the published version of the manuscript.

Funding: The study was carried out with the support of a grant from the Russian Science Foundation (project No. 22-67-00025). The modeling methodology for studying nonlinear flow was developed within the framework of the state assignment of the Ministry of Science and Higher Education of the Russian Federation (FMWN-2025-0007).

Data Availability Statement: Code is provided upon request to the authors.

Conflicts of Interest: The authors declare no conflicts of interest.

References

1. Istomin, V.A.; Yakushev, V.S.; Kvon, V.G.; Dolgaev, S.I.; Chuvilin, E.M. Modern lines in gas hydrate research. *Gazokhimiya* **2009**, *1*, 56–63.
2. Makogon, Y.F. Gas hydrate. Historic background and development prospects. *Geol. Polezn. Iskop. Mirovogo Okeana* **2010**, *2*, 5–21.
3. Sokur, O.N.; Gevorkiyan, V.K. Reserves of hydrocarbons in the 21st century. Methane hydrates of sea basins. *Geol. Polezn. Iskop. Mirovogo Okeana* **2006**, *3*, 52–61.
4. Cheng, C.H.; Redfern, S.A.T. Impact of interannual and multidecadal trends on methane-climate feedbacks and sensitivity. *Nat. Commun.* **2022**, *13*, 3592. [[CrossRef](#)] [[PubMed](#)]
5. Bansal, S.; Post van der Burg, M.; Fern, R.R.; Jones, J.W.; Lo, R.; McKenna, O.P.; Tangen, B.A.; Zhang, Z.; Gleason, R.A. Large increases in methane emissions expected from North America’s largest wetland complex. *Sci. Adv.* **2023**, *9*, eade1112. [[CrossRef](#)] [[PubMed](#)]
6. Mar, K.A.; Unger, C.; Walderdorff, L.; Butler, T. Beyond CO₂ equivalence: The impacts of methane on climate, ecosystems, and health. *Environ. Sci. Policy* **2022**, *134*, 127–136. [[CrossRef](#)]

7. Nisbet, E.G.; Dlugokencky, E.J.; Manning, M.R.; Lowry, D.; Fisher, R.E.; France, J.L.; Michel, S.E.; Miller, J.B.; White, J.W.C.; Vaughn, B.; et al. Rising atmospheric methane: 2007–2014 growth and isotopic shift. *Glob. Biogeochem. Cycles* **2016**, *30*, 1356–1370. [[CrossRef](#)]
8. Schaefer, H.; Fletcher, S.M.; Veidt, C.; Lassey, C.R.; Brailsford, G.W.; Bromley, T.M.; Dlugokencky, E.J.; Michel, S.E.; Miller, J.B.; Levin, I.; et al. A 21st-century shift from fossil-fuel to biogenic methane emissions indicated by $^{13}\text{C}\text{H}_4$. *Science* **2016**, *352*, 80–84. [[CrossRef](#)]
9. Comyn-Platt, E.; Hayman, G.; Huntingford, C.; Chadburn, S.E.; Burke, E.J.; Harper, A.B.; Collins, W.J.; Webber, C.P.; Powell, T.; Cox, P.M.; et al. Carbon budgets for 1.5 and 2 °C targets lowered by natural wetland and permafrost feedbacks. *Nat. Geosci.* **2018**, *11*, 568–573. [[CrossRef](#)]
10. Rosentreter, J.A.; Borges, A.V.; Deemer, B.R.; Holgerson, M.A.; Liu, S.; Song, C.; Melack, J.; Raymond, P.A.; Duarte, C.M.; Allen, G.H.; et al. Half of global methane emissions come from highly variable aquatic ecosystem sources. *Nat. Geosci.* **2021**, *14*, 225–230. [[CrossRef](#)]
11. Kleber, G.E.; Hodson, A.J.; Magerl, L.; Mannerfelt, E.S.; Bradbury, H.J.; Zhu, Y.; Trimmer, M.; Turchyn, A.V. Groundwater springs formed during glacial retreat are a large source of methane in the high Arctic. *Nat. Geosci.* **2023**, *16*, 597–604. [[CrossRef](#)]
12. Milkov, A.V. Global estimates of hydrate-bound gas in marine sediments: How much is really out there? *Earth-Sci. Rev.* **2004**, *66*, 183–197. [[CrossRef](#)]
13. Shakhova, N.; Semiletov, I.; Chuvilin, E. Understanding the permafrost–hydrate system and associated methane releases in the East Siberian Arctic Shelf. *Geosciences* **2019**, *9*, 251. [[CrossRef](#)]
14. Gavrilov, A.; Malakhova, V.; Pizhankova, E.; Popova, A. Permafrost and gas hydrate stability zone of the glacial part of the east-siberian shelf. *Geosciences* **2020**, *10*, 484. [[CrossRef](#)]
15. Chuvilin, E.; Sokolova, N.; Davletshina, D.; Bukhanov, B.; Stanilovskaya, J.; Badetz, C.; Spasennykh, M. Conceptual models of gas accumulation in the shallow permafrost of Northern West Siberia and conditions for explosive gas emissions. *Geosciences* **2020**, *10*, 195. [[CrossRef](#)]
16. Boudreau, B. The physics of bubbles in surficial, soft, cohesive sediments. *Mar. Pet. Geol.* **2012**, *38*, 1–18. [[CrossRef](#)]
17. Liu, H.; Zhan, L.; Lu, H. Mechanisms for upward migration of methane in marine sediments. *Front. Mar. Sci.* **2022**, *9*, 1031096. [[CrossRef](#)]
18. Iversen, N.; Jørgensen, B. Diffusion coefficients of sulfate and methane in marine sediments: Influence of porosity. *Geochim. Cosmochim. Acta* **1993**, *57*, 571–578. [[CrossRef](#)]
19. Luff, R.; Wallmann, K. Fluid flow, methane fluxes, carbonate precipitation and biogeochemical turnover in gas hydrate-bearing sediments at Hydrate Ridge, Cascadia Margin: Numerical modeling and mass balance. *Geochim. Cosmochim. Acta* **2003**, *67*, 3403–3421. [[CrossRef](#)]
20. Xu, W.; Ruppel, C. Predicting the occurrence, distribution, and evolution of methane gas hydrate in porous marine sediments. *J. Geophys. Res. Solid Earth* **1999**, *104*, 5081–5095. [[CrossRef](#)]
21. You, K.; Flemings, P.; Malinverno, A.; Collett, T.; Darnell, K. Mechanisms of methane hydrate formation in geological systems. *Rev. Geophys.* **2019**, *57*, 1146–1196. [[CrossRef](#)]
22. Max, M. Natural gas hydrate. In *Oceanic and Permafrost Environments*; Springer: Berlin/Heidelberg, Germany, 2003; p. 415.
23. Mahabadi, N.; Zheng, X.; Yun, T.; van Paassen, L.; Jan, J. Gas Bubble Migration and Trapping in Porous Media: Pore-Scale Simulation. *J. Geophys. Res. Solid Earth* **2018**, *123*, 1060–1071. [[CrossRef](#)]
24. Paull, C.; Ussler, V., III; Dallimore, S.; Blasco, S.; Lorenson, T.; Melling, H.; Medioli, B.E.; Nixon, F.M.; McLaughlin, F.A. Origin of pingo-like features on the Beaufort Sea shelf and their possible relationship to decomposing methane gas hydrates. *Geophys. Res. Lett.* **2007**, *34*, L01603. [[CrossRef](#)]
25. Serov, P.; Portnov, A.; Mienert, J.; Semenov, P.; Ilatovskaya, P. Methane release from pingo-like features across the South Kara Sea shelf, an area of thawing offshore permafrost. *J. Geophys. Res. Earth Surf.* **2015**, *120*, 1515–1529. [[CrossRef](#)]
26. Chuvilin, E.; Sokolova, N.; Davletshina, D.; Bukhanov, B.; Spasennykh, M. Formation of Gas-Emission Craters in Northern West Siberia: Shallow Controls. *Geosciences* **2021**, *11*, 393. [[CrossRef](#)]
27. Shakhova, N.; Semiletov, I.; Gustafsson, O.; Sergienko, V.; Lobkovsky, L.; Dudarev, O.; Tumskey, V.; Grigoriev, M.; Mazurov, A.; Salyuk, A.; et al. Current rates and mechanisms of subsea permafrost degradation in the East Siberian Arctic Shelf. *Nat. Commun.* **2017**, *8*, 15872. [[CrossRef](#)]
28. Shpak, P.; Turuntaev, S.; Trimonova, M.; Tairova, A.; Belyakov, G.; Iudochkin, N. The model of cohesionless sediment blowout with an increase in the methane flow rate. *Geosciences* **2022**, *12*, 423. [[CrossRef](#)]
29. Trimonova, M.; Shpak, P.; Turuntaev, S.; Tairova, A.; Belyakov, G.; Yudochkin, N. Influence of boundary conditions on initiation of gas blowout in permeable rock. *Env. Geotech.* **2024**, *40*, 1–17. [[CrossRef](#)]
30. Chuvilin, E.; Grebenkin, S.; Sacleux, M. Influence of moisture content on permeability of sandy soils in frozen and unfrozen states. *Cryosphere Earth* **2016**, *20*, 71–78.

31. Chuvilin, E.; Grebenkin, S.; Zhmaev, M. Gas Permeability of Sandy Sediments: Effects of Phase Changes in Pore Ice and Gas Hydrates. *Energy Fuels* **2021**, *35*, 7874–7882. [[CrossRef](#)]
32. Zwicker, D. py-pde: A Python package for solving partial differential equations. *J. Open Source Softw.* **2020**, *5*, 2158. [[CrossRef](#)]

Disclaimer/Publisher’s Note: The statements, opinions and data contained in all publications are solely those of the individual author(s) and contributor(s) and not of MDPI and/or the editor(s). MDPI and/or the editor(s) disclaim responsibility for any injury to people or property resulting from any ideas, methods, instructions or products referred to in the content.